JOURNAL OF SYNCHROTRON RADIATION
ISSN 1600-5775

In situ depth-resolved synchrotron radiation X-ray spectroscopy study of radiation-induced Au deposition

Guang Chen,[a,b] Yonghua Du,[c] Pengfei An,[b] Lirong Zheng,[b] Shengqi Chu[b]* and Jing Zhang[b]*

[a]University of the Chinese Academy of Sciences, Beijing 100049, People's Republic of China, [b]Beijing Synchrotron Radiation Facility, Institute of High Energy Physics, Chinese Academy of Sciences, Beijing 100049, People's Republic of China, and [c]Institute of Chemical and Engineering Sciences, Agency for Science, Technology and Research, 1 Pesek Road, Jurong Island 627833, Singapore. *Correspondence e-mail: chusq@ihep.ac.cn, jzhang@ihep.ac.cn

Received 29 April 2019
Accepted 9 August 2019

Edited by S. M. Heald, Argonne National Laboratory, USA

Keywords: radiation-induced reduction; confocal optic systems; micro-X-ray fluorescence; XANES; deposition processes.

To illustrate the process of synchrotron radiation induced reduction of tetrachloroauric solutions, a confocal synchrotron radiation X-ray spectroscopy experiments system has been introduced to monitor the depth-resolved elemental Au distribution and chemical species during the Au reduction reaction. Combining the results from confocal X-ray spectroscopy with that from X-ray contrast imaging, the mechanism of synchrotron radiation induced Au reduction, along with the process of Au deposition, were proposed. These demonstrations provide novel avenues to spatially resolved analysis of *in situ* solution radiolysis.

1. Introduction

Metal film deposition techniques are critical for their applications in microelectronics, photonics, catalysis, biochemical sensors and so forth (Fukumi *et al.*, 1994; Loo *et al.*, 2005; Chah *et al.*, 2005; Haruta, 1989; Ma *et al.*, 2000). Radiolysis is of significant interest, since it is easier to carry out at room temperature under atmospheric conditions. More importantly, it is independent of the preliminary use of reducing agents, leading to the production of highly pure metals with less contamination (Bharti *et al.*, 2016; Wang *et al.*, 2007). Nowadays synchrotron radiation X-ray radiolysis (Yamaguchi *et al.*, 2016, 2017; Oyanagi *et al.*, 2014; Bharti *et al.*, 2017; Jingyuan *et al.*, 2013; Matsumoto *et al.*, 2015) has become a convenient route for obtaining metal nanostructures with desired sizes, shapes and properties. Bharti *et al.* (2016) explored monochromatic X-ray induced silver nanoparticles for a photovoltaic cell. Ma *et al.* (2000) successfully achieved the formation of a metallic pattern/structure on a substrate, which could help in the development of low-cost test photomasks and microelectronics. Synchrotron radiation induced metal deposition has become a hot topic in the engineering fields.

However, the mechanism of X-ray stimulated processes is still unclear because it is a rapid dynamic chemical process with great heterogeneity in the liquid bulk phase. Early literature suspected that water molecules in solution could be ionized or excited under high-energy X-ray irradiation (Ma *et al.*, 2008; Gachard *et al.*, 1998; Abedini *et al.*, 2013). Heterogeneous charge distribution might exist in the system; the X-ray illuminated volume should be charged more positively than the non-illuminated volume. Complexes such as $AuCl_4^-$ may be driven towards the illuminated area, whereas the activated solvent can supply reducing radicals to neighbouring

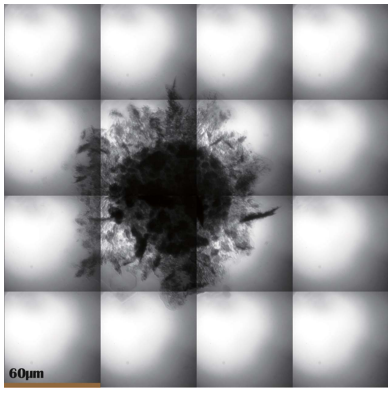

Au ions and contribute to the formation of zero-valence Au (Wang *et al.*, 2007). *In situ* time-resolved X-ray absorption spectroscopy (XAS) was employed to track the reduction of Au ions in aqueous solution in the presence of supporting materials (Ohkubo *et al.*, 2014). This demonstrated that the deposition process depended on the relationship of surface charges between metal ions and supporting materials. Nevertheless, these studies were not available for the spatial chemical speciation distribution which is crucial to our understanding of X-ray stimulated processes.

Micro-X-ray fluorescence (XRF) and XAS are powerful tools for spatially resolved structure analysis via sample mapping in the micrometre regime and have a large variety of fields of application such as environmental sciences, geology, life sciences and archeology. Importantly, the use of confocal X-ray optics, especially capillary optics (Kanngießer *et al.*, 2003), provides a feasible route to analyze geological and cultural heritage samples with depth-resolved chemical speciation of elements (Vekemans *et al.*, 2004; Lühl *et al.*, 2014; Kanngießer *et al.*, 2012; Denecke *et al.*, 2009). In confocal mode, a probing volume is created by the overlapped foci of two optics; the first one is placed in an excitation channel and the second in a detection channel. Confocal detection restricts the probed fraction of the sample to an ellipsoidal volume allowing non-destructive depth-resolved measurements. Confocal micro-X-ray fluorescence is nowadays applied for the measurements of ion distribution near the surface of an electrode, revealing the liquid mass transfer in electrolytic tanks *in situ* (Song *et al.*, 2014). Confocal micro-XAS was also introduced to probe the oxidation states at the cathode/electrolyte interface of an Li ion battery *in operando* (Menzel *et al.*, 2013). This gives important impetus for the developmet of spatially resolved analysis in order to understand the photochemical processes induced by X-ray radiolysis.

In this study, confocal micro-XAS was set up at Beijing Synchrotron Radiation Facility (BSRF). Au ions were irradiated with synchrotron monochromatic X-rays; while confocal micro-XRF monitored the metal ion distribution, confocal micro-XAS examined the oxidation state of metal ions in aqueous solution. By combining the results from confocal X-ray spectroscopy with that from X-ray contrast imaging, the mechanism of synchrotron radiation induced Au deposition was proposed, aiding our understanding of the X-ray stimulated process.

2. Experimental instrumentation

The experiments were performed at the 1W2B beamline of BSRF. A mobile confocal XAS endstation has been developed at this beamline (Chen *et al.*, 2017). The confocal system restricts the probed fraction of the sample to an ellipsoidal volume allowing non-destructive depth-resolved measurements. The confocal element has a 45°/45° geometric design between the first polycapillary parallel half-lens (PCPHL) and the second PCPHL; as shown in Fig. 1, PCPHL was adjusted by a 5D stage. The characteristics of both the PCPHLs are shown in Table 1. In order to perform depth-resolved measurements, the sample holder was placed on a 3D stage. By scanning an Fe knife-edge, the diameter of the focal spot of the first PCPHL (φ_1) and the diameter of the focal spot of the second PCPHL (φ_2) can be obtained; the depth resolution $d_{\rm depth}$ can be approximately determined by φ_1 and φ_2 as follows (Peng *et al.*, 2013),

$$d_{\rm depth} = (\varphi_1 + \varphi_2)/\sqrt{2}.$$

In this work, the depth resolution was around 50 µm at 12 keV. The detector system includes an ionization chamber and a silicon drift detector (SDD). The ionization chamber, fixed in front of the first PCPHL, was used to measure the incident X-ray intensity in order to normalize the fluorescence intensity. The SDD has an energy resolution of about 125 eV at 5.9 keV and maximum count rate of 5.0×10^5 s^{-1}.

An aqueous solution of 1 wt% $HAuCl_4$ was used as the sample and loaded in an in-house-developed cell made from teflon with a thickness of 1.8 mm and a diameter of 5 mm. The cell was sealed tightly with Kapton film to prevent leakage of the liquid. All measurements were carried out at room temperature. The sample cell, filled with $HAuCl_4$ aqueous solution, was placed in the sample holder. When the sample was moved stepwise into the confocal volume, a series of XRF spectra were collected (with an excitation energy of 12.6 keV) and the depth profile was obtained by monitoring the fluorescence intensity of the Au $L\alpha$ peaks (Fig. 2). The sample surface was defined by the peak position of the differential curve of the depth profile (Mantouvalou *et al.*, 2012; Malzer & Kanngießer, 2005). Here, in order to obtain a high-quality fluorescence signal, the point of origin (0 µm) was determined to be at the position of the maximum point of the profile. In the confocal-XRF and X-ray absorption near-edge structure

Table 1
Parameters of PCPHLs.

	Length (mm)	Entrance diameter (mm)	Output diameter (mm)	Focal distance (mm)	Focal spot (µm)/9 keV
First PCPHL	40	5.6	4.3	14	53
Second PCPHL	20.6	5.5	2.6	18	57

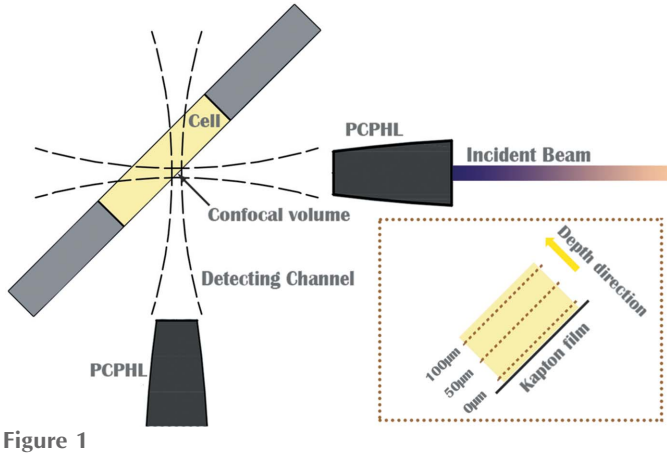

Figure 1
Scheme of the confocal XRF and XAFS system.

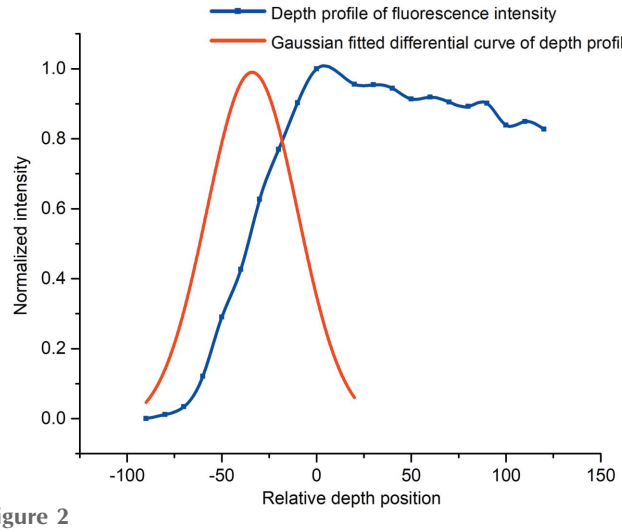

Figure 2
Depth profile of the Au fluorescence intensity.

(XANES) experiments, the confocal probing volume was fixed and the time-dependent Au fluorescence intensity was monitored every 5 min with a integration time of 3 s until it stabilized; the XANES spectrum at the Au L_3-edge was acquired at this point. In order to spatially explore the process of synchrotron radiation X-ray induced Au deposition, three identical $HAuCl_4$ aqueous solutions were prepared and moved to different depth positions at 0 µm, 50 µm and 100 µm. The XRF and XANES experiments were performed on these samples at different probing depths. In the case of self-absorption in fluorescence mode (Lühl *et al.*, 2012), the concentration of the $HAuCl_4$ aqueous solution was no larger than 1 wt%, and no distortion was found in the XAS spectra. The spectra were processed using the program *ATHENA* (Ravel & Newville, 2005), based on the IFEFFIT library (Newville, 2001).

After confocal-XRF and XANES experiments, the deposited Au on Kapton film was characterized by synchrotron radiation 2D X-ray contrast imaging on the 4W1A beamline of BSRF. This beamline provides a monochromatic X-ray flux of 3.5×10^9 photons s^{-1} at 8 keV with a storage ring current of 250 mA. The magnified image was recorded by a 1024×1024 charge-coupled device camera, corresponding to a 60 µm × 60 µm field of view. With an 880-fold magnification and a pixel size of 13.5 µm, one pixel amounts to 15 nm. The exposure time per frame was about 15 s. The sample-to-detector distance was about 30–50 cm. With a computer-controlled rotation stage and a stable mechanical design, the 2D X-ray contrast image can be automatically collected by the computer. The conventional imaging of absorption contrast was used in this experiment.

3. Results and discussion

3.1. Changes in chemical states of elemental Au in the X-ray beam path

Synchrotron monochromatic X-ray irradiation generated reducing agents such as hydrated electrons in the $HAuCl_4$ aqueous solution that undergo chemical reaction: Au^{3+} is transferred to Au. Depth-resolved XANES is applied to investigate the depth dependence of the chemical species of elemental Au and track the reduction of Au ions in aqueous solution. Accordingly, the Au L_3 white-line edge of Au metal is 11922 eV, whereas the white-line edge position of $HAuCl_4{\cdot}3H_2O$ has a −4 eV shift with respect to Au metal (Berrodier *et al.*, 2005). Fig. 3 showed the XANES of the Au L_3-edge at various depths, Au^0 was the main chemical species at depth position 0 µm. A mixture of Au^0 and Au^{3+} existed within the depth at 50 µm. Upon further increasing of the depth position to 100 µm, the main chemical state became Au^{3+}.

3.2. Migration of Au ions in the X-ray beam path

Table 2 shows the counts of Au *Lα* fluorescence intensity at the start and final stable moments for each position. In the beginning, the elemental Au was homogeneous in solution and the fluorescence intensity was almost consistent everywhere when considering the attenuation by the solution. But with increasing radiation time, they varied greatly and Fig. 4 shows their trend in detail. Also, in order to compare the trends at each depth position, the fluorescence intensities were normalized with the respective maximal values. As shown in Fig. 4, the quick rise at 0 µm indicated that the Au precipitation dominated this area. The process tended to stabilize after irradiating for 320 min. With the deeper position, the fluorescence intensity decreased to background within 140 min (depth position 50 µm) and 160 min (depth position 100 µm). These results revealed that X-ray radiation induced the heterogeneous distribution of elemental Au, which migrated

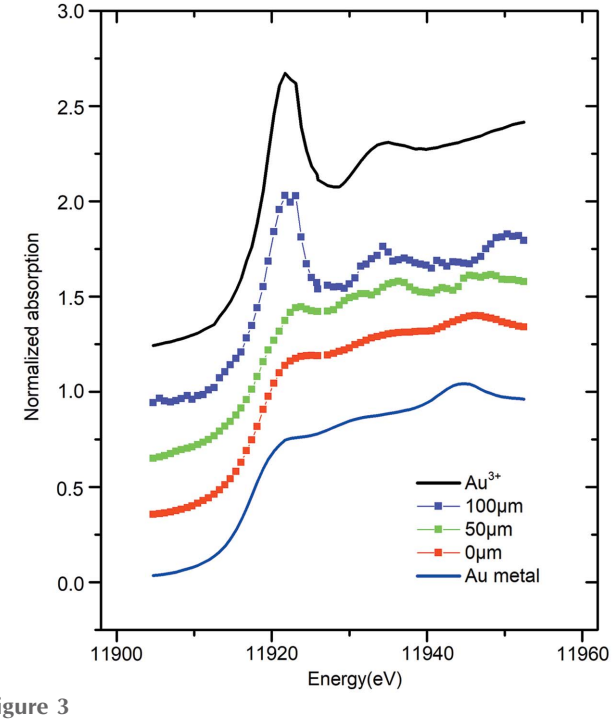

Figure 3
XANES spectrum of the Au L_3-edge at 0 µm, 50 µm and 100 µm.

Table 2
Normalized fluorescence intensity counts with the incident X-ray at the starting and final moment for each position.

Position (μm)	Stable moment	Time (min)	Fluorescence intensity (counts)
0	Start	0	567
	Final	317	33350
50	Start	0	526
	Final	157	127
100	Start	0	499
	Final	174	89

toward the Kapton film window and was deposited on it within the X-ray beam.

3.3. Process of synchrotron radiation induced Au deposition

To further understand Au deposition, we analyzed the 2D X-ray contrast image of deposited Au on the Kapton film window. As shown in Fig. 5, metallic Au was deposited on both the front and back windows. The Au deposition on the front film was significantly circular with a high-density center and slight diffusion around the perimeter. The size of the center is the same as the X-ray full-width spot with a diameter of about 100 μm; whereas on the back film, the Au deposition was dispersed and of low density, which can be explained by the divergence of the PCPHL and the attenuation of the incident beam.

Combining the results from the XANES and XRF analyses, the process of synchrotron radiation induced Au deposition is shown in Fig. 6. X-ray irradiation of water produces reactive radicals and radical ions; the main reducing species are solvated electrons (e^-_{sol}) and hydrogen radicals (Yamaguchi *et al.*, 2016),

$$2H_2O \xrightarrow{Xray} OH^\bullet + H^\bullet + H_3O^+ + e^-_{sol},$$

$$Au^{3+} \xrightarrow{e^-_{sol}} Au.$$

Solvated electrons can easily reduce metal ions down to the zero-valence atoms. As the Au atoms are formed, they act as individual centers of nucleation and further coalescence (Abedini *et al.*, 2013). The acrylic glue on the Kapton film has potential surface adhesion forces to anchor elemental Au from the water phase, which could enhance the coalescence process and metal deposition.

Furthermore, the analysis by XRF indicated that the fluorescence intensity at the origin position (0 μm) was gradually increasing, and XANES shows that metallic

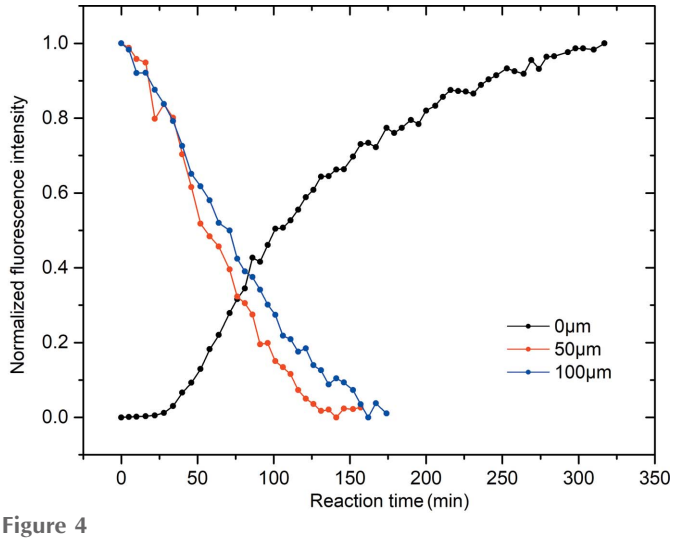

Figure 4
Fluorescence intensity change with radiation time.

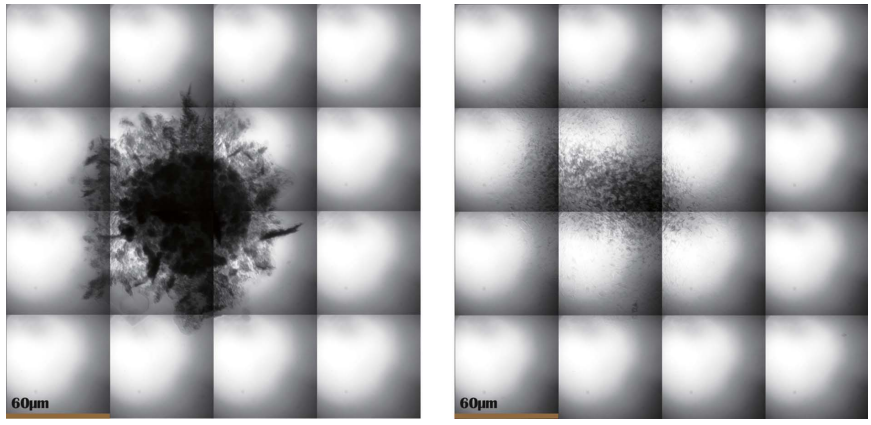

Figure 5
X-ray contrast images of Au deposition on the Kapton film. Left: Au deposition on the front film window. Right: Au deposition on the back film window.

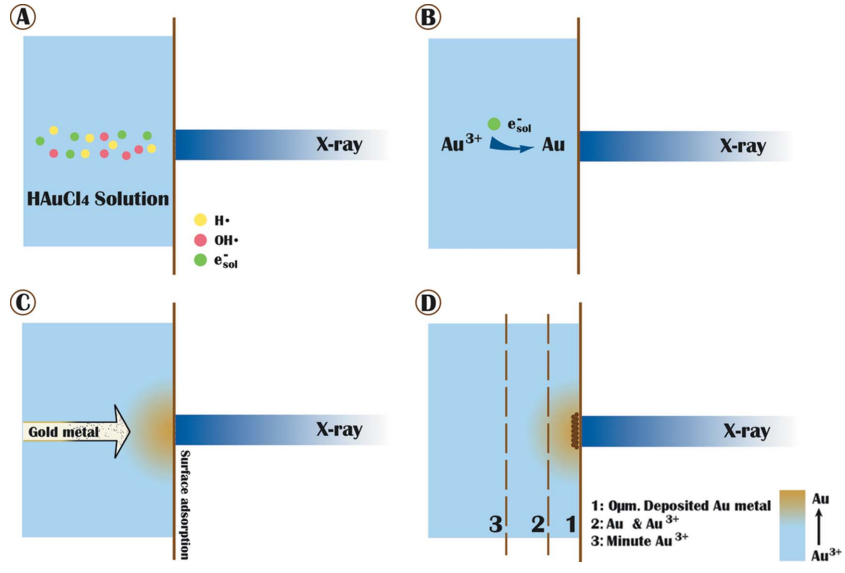

Figure 6
Process of synchrotron radiation induced Au deposition.

Au dominated this area, which was further supported by the high-density image of deposited Au on the front Kapton film window. However, in the deeper layers of the liquid, the beam intensity rapidly decreased; thus, the reduced reaction rate ($Au^{3+} + 3e^{-}_{sol} \rightarrow Au$) could become much slower, and the Au was observed to be deposited on the back film with lower density.

With Au ion migration toward the Kapton film window within the X-ray beam path, a concentration gradient may exist in the water phase; Au^{3+} ions could move from the non-illuminated volume to the illuminated volume. Gradually, with Au deposition on the Kapton film window, the amount of Au ions not only decreased in the water phase, but also the main chemical species was Au^{3+} internally.

4. Conclusions

Confocal XRF and XAS systems were introduced to monitor the heterogeneous reduction process of tetrachloroauric solution via synchrotron radiation. Confocal micro-XRF revealed that X-ray radiation induced the heterogeneous Au distribution. Au migrated into the X-ray illuminated volume and was deposited on the Kapton film. Confocal micro-XANES examined the chemical states of elemental Au in the X-ray beam path following the reduction of Au^{3+} to Au. Furthermore, X-ray contrast imaging of the reduced Au products suggested the Au could be deposited on the Kapton film window via coalescence growth. The feasibility of this approach is demonstrated with the depth-resolved analysis of X-ray induced reduction of tetrachloroauric solutions, and promises to be a wonderful tool for the multi-dimensional analysis of X-ray stimulated processes.

Funding information

We appreciate the financial support from the National Key Research and Development Program of China (grant No. 2017YFA0403402).

References

Abedini, A., Daud, A. R., Hamid, M. A. A., Othman, N. K. & Saion, E. (2013). *Nanoscale Res. Lett.* **8**, 474.
Berrodier, I., Farges, F., Benedetti, M., Winterer, M., Brown, G. E. & Deveughèle, M. (2005). *Geochim. Cosmochim. Acta*, **68**, 3019–3042.
Bharti, A., Agrawal, A. K., Singh, B., Gautam, S. & Goyal, N. (2017). *J. Synchrotron Rad.* **24**, 1209–1217.
Bharti, A., Bhardwaj, R., Agrawal, A. K., Goyal, N. & Gautam, S. (2016). *Sci. Rep.* **6**, 22394.
Chah, S., Hammond, M. R. & Zare, R. N. (2005). *Chem. Biol.* **12**, 323–328.
Chen, G., Chu, S., Sun, T., Sun, X., Zheng, L., An, P., Zhu, J., Wu, S., Du, Y. & Zhang, J. (2017). *J. Synchrotron Rad.* **24**, 1000–1005.
Denecke, M. A., Brendebach, B., De Nolf, W., Falkenberg, G., Janssens, K. & Simon, R. (2009). *At. Spectrosc.* **64**, 791–795.
Fukumi, K., Chayahara, A., Kadono, K., Sakaguchi, T., Horino, Y., Miya, M., Fujii, K., Hayakawa, J. & Satou, M. (1994). *J. Appl. Phys.* **75**, 3075–3080.
Gachard, E., Remita, H., Khatouri, J., Keita, B., Nadjo, L. & Belloni, J. (1998). *New J. Chem.* **22**, 1257–1265.
Haruta, M. (1989). *J. Catal.* **115**, 301–309.
Jingyuan, M., Yang, Z., Zheng, J., Wei, H., Jiong, L., Guozhong, W., Yuying, H. & Hongjie, X. (2013). *Phys. Chem. Chem. Phys.* **15**, 11904–11908.
Kanngießer, B., Malzer, W., Mantouvalou, I., Sokaras, D. & Karydas, A. (2012). *Appl. Phys. A*, **106**, 325–338.
Kanngießer, B., Malzer, W. & Reiche, I. (2003). *Nucl. Instrum. Methods Phys. Res. B*, **211**, 259–264.
Loo, C., Hirsch, L. R., Lee, M.-H., Chang, E., West, J., Halas, N. & Drezek, R. (2005). *Opt. Lett.* **30**, 418–419.
Lühl, L., Hesse, B., Mantouvalou, I., Wilke, M., Mahlkow, S., Aloupi-Siotis, E. & Kanngiesser, B. (2014). *Anal. Chem.* **86**, 6924–6930.
Lühl, L., Mantouvalou, I., Malzer, W., Schaumann, I., Vogt, C., Hahn, O. & Kanngiesser, B. (2012). *Anal. Chem.* **84**, 1907–1914.
Ma, Q., Divan, R., Mancini, D. C. & Keane, D. T. (2008). *J. Phys. Chem. A*, **112**, 4568–4572.
Ma, Q., Moldovan, N., Mancini, D. C. & Rosenberg, R. A. (2000). *Appl. Phys. Lett.* **76**, 2014–2016.
Malzer, W. & Kanngießer, B. (2005). *At. Spectrosc.* **60**, 1334–1341.
Mantouvalou, I., Malzer, W. & Kanngießer, B. (2012). *At. Spectrosc.* **77**, 9–18.
Matsumoto, T., Okada, I., Sakurai, I., Utsumi, Y. & Yamaguchi, A. (2015). *Proceedings of the International Conference on Electronic Packaging & Imaps All Asia Conference (ICEP-IAAC2015)*, 14–17 April 2015, Tokyo, Japan, pp. 866–869.
Menzel, M., Schlifke, A., Falk, M., Janek, J., Fröba, M. & Fittschen, U. E. A. (2013). *At. Spectrosc.* **85**, 62–70.
Newville, M. (2001). *J. Synchrotron Rad.* **8**, 322–324.
Ohkubo, Y., Nakagawa, T., Seino, S., Kugai, J., Yamamoto, T. A., Nitani, H. & Niwa, Y. (2014). *J. Synchrotron Rad.* **21**, 1148–1152.
Oyanagi, H., Orimoto, Y., Hayakawa, K., Hatada, K., Sun, Z., Zhang, L., Yamashita, K., Nakamura, H., Uehara, M., Fukano, A. & Maeda, H. (2014). *Sci. Rep.* **4**, 7199.
Peng, S., Liu, Z., Sun, T., Ma, Y., Sun, W., Zhao, W., He, J., Zhao, G. & Ding, X. (2013). *Nucl. Instrum. Methods Phys. Res. A*, **729**, 565–568.
Ravel, B. & Newville, M. (2005). *J. Synchrotron Rad.* **12**, 537–541.
Song, P., Zhiguo, L., Tianxi, S., Yongzhong, M. & Xunliang, D. (2014). *Anal. Chem.* **86**, 362.
Vekemans, B., Vincze, L., Brenker, F. & Adams, F. (2004). *J. Anal. At. Spectrom.* **19**, 1302–1308.
Wang, C.-H., Chien, C.-C., Yu, Y.-L., Liu, C.-J., Lee, C.-F., Chen, C.-H., Hwu, Y., Yang, C.-S., Je, J.-H. & Margaritondo, G. (2007). *J. Synchrotron Rad.* **14**, 477–482.
Yamaguchi, A., Fukuoka, T., Okada, I., Ishihara, M., Sakurai, I. & Utsumi, Y. (2017). *J. Synchrotron Rad.* **24**, 653–660.
Yamaguchi, A., Okada, I., Fukuoka, T., Ishihara, M., Sakurai, I. & Utsumi, Y. (2016). *Proc. SPIE*, **9929**, 992919.